**Hydrology and
Earth System
Sciences
Discussions**

An application of GLEAM to estimating global evaporation

D. G. Miralles[1], R. A. M. De Jeu[1], J. H. Gash[1], T. R. H. Holmes[1,2], and A. J. Dolman[1]

[1]Department of Hydrology, VU University, Amsterdam, The Netherlands
[2]Hydrology and Remote Sensing Lab, USDA-ARS, Beltsville, MD, USA

Correspondence to: D. G. Miralles (diego.miralles@falw.vu.nl)

HESSD

8, 1–27, 2011

An application of GLEAM to estimating global evaporation

D. G. Miralles et al.

Title Page	
Abstract	Introduction
Conclusions	References
Tables	Figures

◄◄	►►
◄	►
Back	Close

Full Screen / Esc

Printer-friendly Version

Interactive Discussion

An application of GLEAM to estimating global evaporation

D. G. Miralles et al.

Abstract

A physics-based methodology is applied to estimate global land-surface evaporation from multi-satellite observations. GLEAM (Global Land-surface Evaporation: the Amsterdam Methodology) combines a wide range of remotely sensed observations within a Priestley and Taylor-based framework. Daily actual evaporation is derived at quarter degree resolution over the world's land surface. A running water balance of the vertical profile of soil moisture in the root zone is used to estimate the effect of soil water stress on transpiration. Forest rainfall interception, evaporation from bare soil, transpiration and snow sublimation are calculated independently. The inclusion of soil moisture deficit and forest rainfall interception – by means of the Gash analytical model – leads to an improved representation of the magnitude and distribution of the latent heat flux over semiarid and forested regions. Analyses of the global results show that interception loss plays an important role in the partition of the precipitation into evaporation and water available for runoff at a continental scale. The global distribution of evaporation and its different components is analysed to understand the relative magnitude of each component over different ecosystems. This study gives new insights into the relative importance of precipitation and net radiation in driving evaporation, and how the seasonal influence of these controls varies over the different regions of the world. Precipitation is recognised as an important factor driving evaporation, not only in areas that have limited soil water availability, but also in areas of high rainfall interception and low available energy.

1 Introduction

Despite the importance of the latent heat flux as the link between the water, carbon and energy cycles, land-surface evaporation remains one of the most uncertain terms in the world's water balance (Dolman and de Jeu, 2010). Global Climate Model (GCM) estimates of annual volumes range between 58 and 85 10^3 km^3 (Dirmeyer et al., 2006)

and they differ greatly in their global spatial distribution (Jiménez et al., 2009). This creates the need for observation-based evaporation benchmark datasets to evaluate GCM performance (Blyth et al., 2009). Such datasets would help GCM developers to improve their evaporation schemes and consequently their model predictions of future climate.

Jung et al. (2009) presented an approach to upscale eddy-covariance measurements of latent heat flux and produce observation-based global fields of evaporation at monthly timescale. Complementary, satellite observations – able to measure the spatial and temporal variation in the main drivers of evaporation – also contribute a powerful technique to fulfilling the need for accurate global estimates of evaporation. Such estimates have been derived from remote sensing information previously (Choudhury, 1997; Mu et al., 2007; Fisher et al., 2008; Zhang et al., 2010). These studies show that global methodologies require: (a) estimating evaporation at the appropriate temporal and spatial resolution, (b) specifically accounting for soil moisture and its coupling to plant transpiration, and (c) treating forest rainfall interception as an individual process (see Jiménez et al., 2010). Here we satisfy these requirements by using a data-driven (rather than model-driven) approach as described by Miralles et al. (2010b). The methodology, named GLEAM (Global Land-surface Evaporation: the Amsterdam Methodology), is based on the Priestley and Taylor (PT) evaporation formula and the Gash analytical model of forest rainfall interception (Gash, 1979; Valente et al., 1997).

GLEAM uses an extensive range of independent remotely-sensed observations as a basis for estimating daily actual evaporation (and its different components) at a global scale and quarter-degree spatial resolution. The approach is physics-based and although it contains some empirical parameters these have been derived from the results of separate field studies; calibration or tuning of new parameters is thus unnecessary. The explicit coupling between evaporation and soil moisture conditions and the separate estimation of rainfall interception allow application of the methodology in land-atmosphere feedback studies and tests of GCM performance. The evaporation product has been successfully validated over different vegetation and climate conditions using

An application of GLEAM to estimating global evaporation

D. G. Miralles et al.

Title Page

Abstract | Introduction

Conclusions | References

Tables | Figures

◄ | ►

◄ | ►

Back | Close

Full Screen / Esc

Printer-friendly Version

Interactive Discussion

in situ observations from 43 stations of the FLUXNET global network of micrometeorological flux measurements (see Miralles et al., 2010b).

Here, GLEAM is first applied at a watershed scale to validate the estimated long-term partitioning of incoming precipitation (P) into evaporation (E) and water available for runoff ($P-E$) using observations of river discharge from the Global Runoff Data Centre (GRDC). The methodology is then applied at a global scale to study the global distribution of land evaporation and its different components. The role of rainfall interception and soil moisture on both the long-term partitioning of precipitation, and the seasonal distribution of the main drivers of evaporation (i.e. net radiation and soil moisture), is analysed in detailed.

2   The GLEAM framework

The methodology is driven by a large set of remote sensing observations from different satellites (see Miralles et al., 2010b for a detailed description of the different input data sets and full details of the methodology). GLEAM produces daily estimates of global evaporation at a 0.25° spatial resolution. It is structured in four interconnected units (see Fig. 1): (a) the interception model, (b) the soil water module, (c) the stress module, and (d) the PT module. The scheme is independently formulated for three land surface types with specific physical characteristics: (a) land covered by tall canopies, (b) land covered by short vegetation, and (c) bare soil.

The estimation of forest rainfall interception is based on the revised version of Gash's analytical model (Valente et al., 1997). It calculates daily estimates of global canopy rainfall interception loss (I) using remotely-sensed observations of precipitation (P) and forest cover. The interception component of GLEAM is described in detail by Miralles et al. (2010a).

The soil water module consists of a multilayer bucket model driven by P and calculating soil moisture for different layers within the root-zone. Satellite-measured surface soil moisture is assimilated into the first layer of the profile by means of a Kalman filter.

4

The Kalman filter is based on the uncertainty of the soil moisture observations, which is given by the satellite-derived vegetation optical depth (the higher the optical depth, the higher the uncertainty in surface soil moisture observations – see De Jeu et al., 2008). Optimised estimates of soil moisture (θ) are subsequently translated into estimates of evaporative stress represented by a factor (S), ranging from 0 (maximum stress) to 1 (no stress). PT estimates of potential evaporation are multiplied by S to estimate plant transpiration (in vegetated cover) and bare soil evaporation. The final estimate of actual evaporation for each pixel is the result of aggregating the fluxes from the three different land cover types (tall canopy interception loss, tall canopy transpiration, short vegetation transpiration, bare soil evaporation) weighted by the percentage of each cover type within the pixel. In pixels covered by ice and snow, E is independently calculated by adapting the PT equation to estimate sublimation as described by Murphy and Koop (2005).

3 Validation of the volumes of water available for runoff

Model estimates of the volume of water available for runoff ($P - E$) have been compared to station-based river discharge measurements from the Global Runoff Data Centre (GRDC) in Koblenz, Germany. This large-scale validation of GLEAM is complementary to the validations of the independent modules described by Miralles et al. (2010a,b).

Estimates of P used in GLEAM (both in the interception model and the soil moisture module) are normally derived from the Climate Prediction Center morphing technique precipitation product (CMORPH – Joyce et al., 2004). This precipitation product is based only on satellite observations and has a high spatial resolution (0.07°). Previous studies have shown that CMORPH is in better agreement with in situ observations than the majority of existing precipitation products (see Ebert et al., 2007). However, CMORPH presents two practical disadvantages when applied in GLEAM: (a) its spatial domain (60° N–60° S) does not cover the entire globe, and (b) the product tends to underestimate snowfall (see Zeweldi and Gebremichael, 2009). Consequently, the 1°

Full Screen / Esc

Printer-friendly Version

Interactive Discussion

resolution Global Precipitation Climatology Project (GPCP) product (Huffman et al., 2001) is used to fill this gap in CMORPH coverage, and also in snow-covered pixels.

For the period 2003–2006, Fig. 2 shows the results of the comparison between GLEAM catchment estimates of $P-E$ and river runoff measurements from 24 rivers (see Table 1 for the description of the river basins). Catchments were selected according to the availability of GRDC data during the complete study period and only rivers with an average annual discharge larger than $20 \, \text{km}^3$ were considered for the study. Due to the obvious sensitivity of the $P-E$ estimates to errors in the precipitation product, the analysis was repeated using only GPCP data as P (instead of the usual blended product based on CMORPH and explained above). Note that the choice of precipitation product implicitly affects the calculation of E, despite the fact that the sensitivity of E to values of P is much lower than the sensitivity of $P-E$ estimates (this can be noted in Table 1). Figure 2 shows the statistics of the correlation when the methodology is run with CMORPH ($R = 0.70$, MBE $= -8.8 \, \text{mm yr}^{-1}$) and when it is run with GPCP ($R = 0.85$, MBE $= 46.5 \, \text{mm yr}^{-1}$). The higher correlation coefficient found for the GPCP-based $P-E$ estimates can be explained by the high positive bias of the CMORPH-based $P-E$ estimates in the rivers of central United States (see Table 1). This is in agreement with the findings of Tian et al. (2007), who reported a clear overestimation of CMORPH rainfall during the warm season in this area.

GLEAM is not a tuned or calibrated hydrological model and Fig. 2 should therefore be interpreted with a consideration of the magnitude and different origins of the various uncertainties. Because river discharge estimates are usually derived from a stage-discharge rating curve, they include the errors in the measurements of river height and in the discharge data used to calibrate the rating curve, as well as the errors from the interpolation and extrapolation due to changes in river bed roughness, hysteresis effects, etc (see Di Baldassarre and Montanari, 2009). On top of those, the volumes in the vertical axes are also affected by the uncertainties in the estimation of the discharge-contributing area (given that the observations are presented in mm). On the vertical axes, the uncertainty in $P-E$ estimates will result from the uncertainty

associated with the precipitation product and with GLEAM estimates of land evaporation (which includes the errors in the satellite data used to drive the methodology, the scaling of those to the desired 0.25° resolution, and the model structure itself – see Miralles et al., 2010b). Despite all these possible sources of uncertainty a level of correlation remains as seen in Fig. 2; moreover, the $P-E$ estimates are in the right order of magnitude and overall lack a systematic bias.

The correlation in Fig. 2 depends on the validity of three assumptions: (a) the entire volume of river water extracted for human use returns to the river, (b) the catchment is water-tight, and (c) both the lag-time between a rainfall peak in the watershed and the discharge peak in the measuring station, and the long-term change in soil water storage, can be neglected by considering a relatively long (4 year) period.

The assumption (a) implicitly neglects the increase of transpiration caused by irrigation. Therefore, an underestimation of E in catchments with intense irrigation could be responsible for the scatter. To test this hypothesis, the FAO Global Map of Irrigation Areas (Siebert et al., 2005) – that presents irrigation area as a percentage of the total area – was combined with GLEAM estimates of potential evaporation under the assumption that irrigated land evaporates at potential rate. This consideration had little impact in the scatter, resulting only in a slight improvement of the statistics shown in Fig. 2 ($R = 0.71$, MBE $= -13.2\,\mathrm{mm\,yr^{-1}}$, and $R = 0.86$, MBE $= 41.1\,\mathrm{mm\,yr^{-1}}$ for CMORPH and GPCP, respectively). A global analysis of the distribution of $P-E$ estimates is presented in Sect. 4.1; as in previous applications of GLEAM (i.e. Miralles et al., 2010a,b), the CMORPH-based P is chosen for the global run of the methodology. This choice is mainly justified by the better resolution of CMORPH compared to GPCP.

4   Results of the global application of GLEAM

The methodology has been applied globally for the period 2003–2007 using the satellite data products listed by Miralles et al. (2010b) as driving data. Results are analysed

in terms of the magnitude of evaporation at a continental scale and the range of variation of the flux (and its separate components) over the different ecosystems. Special emphasis is given to the role of interception loss in the long-term recycling of land precipitation and its repercusions on runoff generation. The daily time-resolution of the model allows a correspondingly high resolution analysis of the temporal correlations between evaporation and external factors limiting the flux; an analysis of the distribution and seasonality of these correlations is also presented. Results underline the importance of the accurate estimation of the flux of wet canopy evaporation and the coupling between soil moisture and transpiration if we are to understand the dynamics and trends of evaporation over the complete globe.

4.1 Long-term partition of precipitation

For a certain region, and over a sufficiently long period to allow the net change of water storage in the soil to be neglected, the land-incoming precipitation is either recycled back into the atmosphere through evaporation, or it drains into the water bodies in the region. Figure 3 presents a graphic overview of the global partitioning of precipitation over land according to GLEAM. The total volumes of the different hydrological fluxes across the latitudinal bands are illustrated for the period 2003–2007. All the fluxes are larger close to the Equator due to the higher average incoming radiation, temperature and specific humidity.

Table 2 shows the volumes of total precipitation (P), evaporation (E, which includes transpiration, soil evaporation, snow sublimation and forest interception loss), and water available for runoff ($P-E$) for each continent. The right-hand columns present the contribution of forest rainfall interception (I) to the long-term partitioning of P into E and $P-E$. The volume of annual global land-surface evaporation is estimated as 67×10^3 km^3. Forest interception loss amounts to 10% of the global evaporation or 6% of the continental precipitation. All the fluxes are higher in South America due to the faster dynamics of the hydrological cycle over Amazonia.

To better understand the role of I in the partitioning of incoming precipitation over forested ecosystems, the land-use classification scheme of the International Geosphere-Biosphere Programme (IGBP) is used in Table 3 to present the same hydrological fluxes allocated to biome types. Given that I is calculated for the fraction of tall canopy within each pixel, it can still occur within pixels in which the dominant land use is not forest. Tropical forests contribute to 30% of the global land-surface evaporation and 57% of the global canopy interception loss. In these ecosystems, 20% of the evaporation corresponds to the flux of rainfall interception loss; this flux is equivalent to 18% of the water available for river discharge. At higher latitudes the relative contribution of forest interception to land-surface evaporation is also large. In temperate forests, the volume of rainfall interception is on average 13% of the incoming precipitation (17% of the total evaporation).

4.2 Spatial distribution of evaporation and its different components

The global distribution of the average annual evaporation during the period 2003–2007 is presented in Fig. 4. Different components of the flux are shown independently to give an idea of the relative importance of each of them over the different ecosystems. Transpiration contributes to the majority of the global land evaporation and it is especially large in the humid tropics due to the sufficient availability of soil moisture during the entire year and the close dependency of transpiration on the incoming radiation. The contribution of canopy interception to the global volume of evaporation is larger than the contribution from bare soil evaporation and snow sublimation. Evaporation from bare soil is important in desert regions even though it only happens during (and shortly after) the sporadic rainfall events. Peaks of snow sublimation occur in the Himalayas where annual net radiation is higher than in other permanent snow-covered areas due to its low latitude.

Figure 5 shows the global maps of E, I and $P-E$ for the period 2003–2007. The months of June, July and August (JJA), and December, January and February (DJF) are displayed separately to illustrate the seasonal variations in the fluxes. These

An application of GLEAM to estimating global evaporation

D. G. Miralles et al.

Title Page

Abstract	Introduction
Conclusions	References
Tables	Figures

◄◄   ►►

◄   ►

Back   Close

Full Screen / Esc

Printer-friendly Version

Interactive Discussion

seasonal patterns of E, I and $P-E$ indicate the relative importance of evaporation in the availability of water for runoff at different times of the year. While the global distribution of runoff generation is dominated by the seasonal cycle of precipitation, over most of the world the land-surface evaporation is dominated by the seasonal cycle of net radiation (see also Sect. 4.3). The largest seasonal variations in E are found in subtropical areas with sufficient soil water content during the summer period; in some of these regions the volume of E in summer-time can become almost one order of magnitude larger than during the winter (see for instance Northern Australia, Southern Africa or the east coast of United States). Regions where the soil moisture content is low throughout the entire year (like central Australia or the Arabian Peninsula) present a low range in the seasonality of E, which is independent of the cycle of R_n.

4.3 Insight into the evaporation drivers

The main factors that limit land evaporation are the available energy and the volume of precipitation. The spatial and temporal distribution of these limiting factors, and the strength of the correlation of evaporation with one particular driver, can provide valuable information on the seasonal dynamics of evaporation in a particular area. Teuling et al. (2009) hypothesised that regional trends in land evaporation respond to trends in the limiting drivers. Only when we know to what extent a specific driver is controlling the evaporation process, may known changes in that controlling factor be translated into long-term changes in evaporation.

GLEAM can be applied to estimate the strength of the relationship between land evaporation and its external drivers at a global scale. Figure 6 gives a global overview of such analysis for the period 2003–2007. Figure 6a shows the global distribution of the correlation coefficient between daily time series of E and R_n and the correlation coefficient between E and θ – estimated as the volumetric water content for the whole root-zone – for JJA as averaged over the five year period. Figure 6b shows the same inferences for the period DJF. Figure 6c,d presents the global distribution of the correlation between E and R_n, and E and P for JJA and DJF, respectively. The model

predicts that most of the summer-time daily variability of E over Central Europe and North America can be explained by the dynamics in R_n (see high correlation between E and R_n in Fig. 6a). In winter-time the relation with R_n is weaker and P becomes an important controlling factor due to the enhanced relative importance of interception loss (see Fig. 6d). As expected, areas presenting high correlations between E and θ correspond mainly to arid and semiarid regions, and especially during summer-time (see Fig. 6a,b).

5 Discussion

The average annual land-surface evaporation estimated by GLEAM for the period 2003–2007 is 67×10^3 km^3, which is comparable to other estimates of average annual land evaporation – e.g. the 71×10^3 km^3 found by Baumgartner and Reichel (1975) (see Dolman and Gash, 2010) or the 66×10^3 km^3 found by Jung et al. (2010) – and within the range of values reported by Dirmeyer et al. (2006) for different GCMs. Fisher et al. (2008) reported similar results (both in absolute and in relative terms) to the ones presented in Fig. 3 for the annual volumes of precipitation and evaporation. The latitudinal profile of the fluxes is in agreement with the hypothesis that, when considering interception loss, evaporation can reach and even exceed the available energy, especially at high latitudes where the available energy is low (Stewart, 1977). In addition, canopy interception represents a net loss of water available for runoff, and can be equivalent to 20% of river discharge (see also Fig. 5d,f). Humid tropics show a value of land evaporation around 50% of the incoming precipitation, in accordance with the level of rainfall recycling in these areas reported by Salati and Vose (1984).

Figure 5b,d shows how at higher latitudes in winter-time, when the net radiation is low, the flux of interception loss – dominated by the aerodynamic forces rather than by the available energy – can represent the main source of land-surface evaporation in forested regions. The different bio-physical processes behind interception loss and transpiration make wet canopy evaporation more dependent on the volume

and duration of rainfall and less on the net radiation (see Shuttleworth and Calder, 1979). Under low energy availability, rates of wet canopy evaporation can become several times higher than the rates of transpiration that would be occurring under dry conditions (see commentary by Gash and Shuttleworth, 2007). In the context of the Penman-Monteith equation, the aerodynamic term (and not the energy one) is respon-5 sible for the major part of the flux. This is the main reason why interception loss requires a separate estimation, and why PT energy-based approaches are not suitable for its estimation.

Traditionally, studies on evaporation drivers have been focused on net radiation and 10 soil moisture (considered as the link between precipitation and evaporation). However, an important component of the evaporative flux from forests, canopy-intercepted rainfall, will not be directly affected by the soil moisture dynamics. Moreover, as stated above, the flux of evaporated water from wet canopies is relatively independent from the net radiation. Figure 6a,c shows how in summer-time and over Central Europe and 15 North America, most of the variability of daily E can be explained by the dynamics in R_n. This is in agreement with Fig. 5a,b, that illustrate how in the majority of the world's land surface the seasonality of the validated GLEAM estimates of E follows closely the seasonality of the incoming solar energy. However, in forested regions and during winter-time the relationship is not obvious (see Fig. 6b,d). This low dependency of the 20 time series of E on the time series of R_n is a response to the higher relative importance of I as a component of E, given the low volumes of transpiration in winter-time. As can be appreciated from Fig. 6d, in forested regions under conditions of low incoming radiation, the model identifies the availability of water on the canopy (dominated by the volume of P and its duration) as an important factor determining the dynamics of 25 evaporation. The low correlations found with θ over the same areas, suggest that the correlation with P is not a response to conditions of soil water deficit. For tropical rain forests, despite the fact that R_n remains in general the largest controlling factor, P is also an important driver of evaporation in both seasons.

Trends in soil moisture can be responsible for the long-term changes in land evaporation; this happens over regions where water availability is the main control on the evaporation (see Teuling et al., 2009). Jung et al. (2010) analysed the results of their FLUXNET data-based approach (Jung et al., 2009) to reveal a positive trend in global land-surface evaporation from 1982 to 1997, but from 1998 this trend slowed down, attributed to the decrease in soil moisture over the Southern Hemisphere. Blue-coloured regions in Fig. 6a,b represent the areas where GLEAM identifies that a long-term decrease in soil moisture could potentially induce a negative trend in land evaporation. They are mainly arid and semiarid regions, where the rate of actual evaporation rarely matches the potential rate (especially during summer-time) and it is the availability of water in the soil that will determine the volume of daily evaporation. This dependency on the soil moisture underlines the importance of correctly parameterising the soil water content and the stress conditions for those areas.

A comparison between Fig. 6c and d shows that in arid regions the correlation of E with the time series of P is lower than the correlation between E and θ; this is because soil moisture is a more direct indicator of plant water stress. However, when comparing Fig. 6a with c or Fig. 6b with d, one should consider how values of P affect the estimation of θ. The sensitivity of θ to P will be higher in areas and periods of dense vegetation. This happens because the satellite-derived vegetation optical depth is used to quantify the errors in the microwave soil moisture observations during their assimilation (see Sect. 2). In arid and semiarid areas the optical depth will be lower, and therefore the final estimates of θ will be more sensitive to the satellite soil moisture observations and less sensitive to the values of P than in more vegetated regions. Nevertheless, as Fig. 6a,b shows, the correct estimation of soil moisture is more significant in sparsely-vegetated areas where the estimates of satellite-based soil moisture (and therefore also the estimates of θ) are less uncertain. As noted above, in forested areas where P is important, E remains relatively uncorrelated with θ; this happens in spite of the higher dependency of θ on the values of P in those areas. This suggests that the soil remains under no stress for transpiration, reflecting the low stomatal conductance

and deep roots of trees, which have evolved to survive droughts. GLEAM accounts for these processes through the forest values of the Priestley and Taylor alpha coefficient, the stress parameterisation and the rooting depth. The component of forest evaporation that is affected by P (and governing the dynamics of E) is therefore not the transpiration flux but the rainfall interception loss.

6 Conclusions

GLEAM provides reliable estimates of global evaporation and its different components by combining satellite-observable variables within a simple bio-physical approach. It fills the gaps from previous satellite-based evaporation models acknowledging the importance of estimating interception loss through a widely-tested model (Gash's analytical model), and moderating PT estimates of latent heat flux by considering the soil water stress conditions over the entire root-zone. As with every model, GLEAM is a simplification of reality: results presented here are affected by the assumptions taken in the parameterisation of the bio-physical processes within the methodology. However, the constituent parts of GLEAM have been successfully validated by comparison with in situ data over different ecosystems conferring credibility on the results presented in this paper.

An average annual land evaporation of 67×10^3 km^3 was found for the period 2003–2007, which represented 58% of the incoming precipitation. Canopy interception loss contributed to 10% of the global evaporation (6% of the precipitation) playing a major role in the long-term partition of rainfall and the volume of runoff generated in forested ecosystems. Precipitation was identified as an important factor driving evaporation in forested regions due to the effect of evaporation of canopy-intercepted rainfall – a process which is relatively independent of net radiation and occurs at a higher rate than transpiration. The methodology also located soil moisture limited regions in which long-term trends on land evaporation are likely respond to trends in soil available water.

Following plans include the application of GLEAM to develop a 24 year database (from 1984 to 2007) and an inter-product comparison with existing global fields of evaporation within the LandFlux-EVAL initiative of the GEWEX Radiation Panel (see Jiménez et al., 2010). The product could additionally be used to investigate trends in land evaporation and their relation to ocean oscillations, the effects of land-use changes such as desertification or deforestation on the hydrological cycle, and the coupling between land and atmospheric processes.

All GLEAM products will become freely available through the web portal hosted at the VU University Amsterdam Geo-services website (http://geoservices.falw.vu.nl).

References

Baumgartner, A. and Reichel, E.: The World Water Balance: Mean Annual Global Continental and Maritime Precipitation, Evaporation and Runoff, Elsevier Scientific Publishing Company, Amsterdam, The Netherlands, Oxford, UK and New York, USA, 1975.

Blyth, E. M., Shuttleworth, W. J, and Harding, R. J.: Summary of the GEWEX International Symposium on Global Land-surface Evaporation and Climate, Hydrol. Process., 23, 3411–3412, 2009.

Choudhury, B. J. and DiGirolamo, N. E.: A biophysical process-based estimate of global land surface evaporation using satellite and ancillary data; I. Model description and comparison with observations, J. Hydrol., 205, 164–185, 1998.

De Jeu, R. A. M., Wagner, W., Holmes, T. R. H., Dolman, A. J., van de Giesen, N. C., and Friesen, J.: Global soil moisture patterns observed by space borne microwave radiometers and scatterometers, Surv. Geophys., 29, 399–420, 2008.

Di Baldassarre, G. and Montanari, A.: Uncertainty in river discharge observations: a quantitative analysis, Hydrol. Earth Syst. Sci., 13, 913–921, doi:10.5194/hess-13-913-2009, 2009.

Dirmeyer, P. A., Gao, X. A., Zhao, M., Guo, Z. C., Oki, T., and Hanasaki, N.: GSWP-2 Multimodel anlysis and implications for our perception of the land surface, B. Am. Meteorol. Soc., 87, 1381–1397, 2006.

Dolman, A. J. and De Jeu, R. A. M.: Evaporation in focus, Nat. Geosci., 3, 296, 2010.

Dolman, A. J. and Gash, J. H.: Evaporation in the global hydrological cycle, in: Treatise on Water Science, edited by: Wilderer, P., vol. 2, chapt. 5, Elsevier, in press, 2010.

Ebert, E. E., Janowiak, J. E., and Kidd, C.: Comparison of near-real time precipitation estimates from satellite observations and numerical models, B. Am. Meteorol. Soc., 88, 47–64, 2007.

Fisher, J. B., Tu, K. P., and Baldocchi, D. D.: Global estimates of the land-atmosphere water flux based on monthly AVHRR and ISLSCP-II data, validated at 16 FLUXNET sites, Remote Sens. Environ., 112, 901–919, 2008.

Gash, J. H.: An analytical model of rainfall interception by forests, Q. J. Roy. Meteorol. Soc., 105, 43–55, 1979.

Gash, J. H. and Shuttleworth, W. J.: Vegetation controls on evaporation – commentary, in: Benchmark Papers in Hydrology: Evaporation, edited by: Gash, J. H. and Shuttleworth, W. J., IAHS Press, Wallingford, 233–239, 2007.

Huffman, G. J., Adler, R. F., Morrissey, M. M., Bolvin, D. T., Curtis, S., Joyce, R., McGavock, B., and Susskind, J.: Global precipitation at one-degree daily resolution from multisatellite observations, J. Hydrometeorol., 2, 36–50, 2001.

Jiménez, C., Prigent, C., and Aires, F.: Toward an estimation of global land surface heat fluxes from multisatellite observations, J. Geophys. Res.-Atmos., 114, D06305, doi:10.1029/2008JD011392, 2009.

Jiménez, C., Prigent, C., Mueller, B., Seneviratne, S. I., McCabe, M. F., Wood, E. F., Rossow, W. B., Balsamo, G., Betts, A. K., Dirmeyer, P. A., Fisher, J. B., Jung, M., Kanamitsu, M., Reichle, R. H., Reichstein, M., Rodell, M., Sheffield, J., Ku, T., and Wang, K.: Global inter-comparison of 12 land surface heat flux estimates, J. Geophys. Res.-Atmos., in press, 2010.

Joyce, R. J., Janowiak, J. E., Arkin, P. A., and Xie, P.: CMORPH: A method that produces global precipitation estimates from passive microwave and infrared data at high spatial and temporal resolution, J. Hydrometeorol., 5, 487–503, 2004.

Jung, M., Reichstein, M., and Bondeau, A.: Towards global empirical upscaling of FLUXNET eddy covariance observations: validation of a model tree ensemble approach using a biosphere model, Biogeosciences, 6, 2001–2013, doi:10.5194/bg-6-2001-2009, 2009.

An application of GLEAM to estimating global evaporation

D. G. Miralles et al.

Jung, M., Reichstein, M., Ciais, P., Seneviratne, S., Sheffield, J., Goulden, M., Bonan, G., Cescatti, A., Chen, J., de Jeu, R., Dolman, A. J., Eugster, W., Gerten, D., Gianelle, D., Gobron, N., Heinke, J., Kimball, J., Law, B., Montagnani, L., Mu, Q., Mueller, B., Oleson, K., Papale, D., Richardson, A., Roupsard, O., Running, S., Tomelleri, E., Viovy, N., Weber, U., Williams, C., Wood, E., Zaehle, S., and Zhang, K.: Recent decline in the global land evapotranspiration trend due to limited moisture supply, Nature, 467, 951–954, doi:10.1038/nature09396, 2010.

Miralles, D. G., Gash, J. H., Holmes, T. R. H., De Jeu, R. A. M., and Dolman, A. J.: Global canopy interception from satellite observations, J. Geophys. Res.-Atmos., 115, D16122, doi:10.1029/2009JD013530, 2010a.

Miralles, D. G., Holmes, T. R. H., De Jeu, R. A. M., Gash, J. H., Meesters, A. G. C. A., and Dolman, A. J.: Global land-surface evaporation estimated from satellite-based observations, Hydrol. Earth Syst. Sci. Discuss., 7, 8479–8519, doi:10.5194/hessd-7-8479-2010, 2010b.

Mu, Q., Heinsch, F. A., Zhao, M., and Running, S. W.: Development of a global evapotranspiration algorithm based on MODIS and global meteorology data, Remote Sens. Environ., 111, 519–536, 2007.

Murphy, D. M. and Koop, T.: Review of the vapour pressures of ice and supercooled water for atmospheric applications, Q. J. Roy. Meteorol. Soc., 131, 1539–1565, 2005.

Salati, E. and Vose, P. B.: Amazon Basin: a system in equilibrium, Science, 225, 129–138, 1984.

Shuttleworth, W. J. and Calder, I. R.: Has the Priestley-Taylor equation any relevance to forest evaporation?, J. Appl. Meteorol., 18, 639–646, 1979.

Siebert, S., Döll, P., Hoogeveen, J., Faures, J.-M., Frenken, K., and Feick, S.: Development and validation of the global map of irrigation areas, Hydrol. Earth Syst. Sci., 9, 535–547, doi:10.5194/hess-9-535-2005, 2005.

Stewart, J. B: Evaporation from the wet canopy of a pine forest, Water Resour. Res., 13, 915–921, 1977.

Teuling, A. J., Hirschi, M., Ohmura, A., Wild, M., Reichstein, M., Ciais, P., Buchmann, N., Ammann, C., Montagnani, L., Richardson, A. D., Wohlfahrt, G., and Seneviratne, S. I.: A regional perspective on trends in continental evaporation, Geophys. Res. Lett., 36, L02404, doi:10.1029/2008GL036584, 2009.

Tian, Y., Peters-Lidard, C. D., Chaudhury, B. J., and Garcia, M.: Multitemporal analysis of TRMM-based satellite precipitation products for land data assimilation applications, J. Hydrometeorol., 8, 1165–1183, 2007.

Valente, F., David, J. S., and Gash, J. H.: Modelling interception loss for two sparse eucalypt and pine forests in Central Portugal using reformulated Rutter and Gash analytical models, J. Hydrol., 190, 141–162, 1997.

Zeweldi, D. A. and Gebremichael, M.: Evaluation of CMORPH precipitation products at fine space-time scales, J. Hydrometeorol., 10, 300–308, 2009.

Zhang, K., Kimball, J. S., Nemani, R. R., and Running, S. W.: A continuous satellite-derived global record of land surface evapotranspiration from 1983 to 2006, Water Resour. Res., 46, W09522, doi:10.1029/2009WR008800, 2010.

An application of GLEAM to estimating global evaporation

D. G. Miralles et al.

Title Page

Abstract	Introduction
Conclusions	References
Tables	Figures

◀ ▶|

◀ ▶

Back Close

Full Screen / Esc

Printer-friendly Version

Interactive Discussion

Table 1. GRDC stations used in the comparison of $P-E$ and observed annual river runoff (Q). Results correspond to the period 2003–2006.

River	Location of the station			Area (10^3 km^2)	Q (mm)	$P-E$ (mm)		E (mm)	
	Lat (deg)	Long (deg)	Country			CMORPH	GPCP	CMORPH	GPCP
Alabama	7.80	6.77	USA	55.6	581	647	645	896	905
Apalachicola	29.95	−85.02	USA	49.7	443	506	603	902	918
Arkansas	34.79	−92.36	USA	409.3	83	370	120	745	641
Columbia	46.18	−123.18	USA	665.4	284	73	205	461	469
Danube	45.22	28.72	Romania	807.0	296	221	455	430	457
Elbe	53.23	10.89	Germany	132.0	151	119	445	316	352
Fraser	49.38	−121.45	Canada	217.0	361	172	369	447	512
Glomma	59.61	11.12	Norway	40.5	501	681	655	259	285
Liard	61.75	−121.22	Canada	275.0	284	171	155	363	393
Mackenzie	67.46	−133.74	Canada	1660.0	177	94	94	327	348
Mississippi	37.22	−89.46	USA	1847.2	81	329	189	534	496
Missouri	38.71	−91.44	USA	1357.7	37	297	110	533	476
Nelson	56.40	−94.37	Canada	1060.0	105	121	159	372	411
Niger	7.80	6.77	Nigeria	1331.6	125	378	152	370	329
Ohio	38.28	−85.80	USA	236.1	570	442	624	631	650
Rhine	51.84	6.11	Netherlands	160.8	378	128	521	394	439
St. Lawrence	45.42	−73.62	Canada	959.1	265	130	476	460	548
Snake	46.10	−116.98	USA	240.8	107	67	63	464	386
Susquehanna	39.66	−76.18	USA	70.2	697	373	758	572	629
Tanana	64.57	−149.09	USA	66.3	346	267	248	293	312
Tennessee	35.23	−88.26	USA	85.8	822	799	669	795	793
Tombigbee	31.76	−88.13	USA	47.7	641	700	565	931	935
Wabash	38.40	−87.75	USA	74.2	424	522	671	575	581
Yukon	61.93	−162.88	USA	831.4	254	195	180	294	310

Title Page

Abstract | Introduction

Conclusions | References

Tables | Figures

◄ | ►

◄ | ►

Back | Close

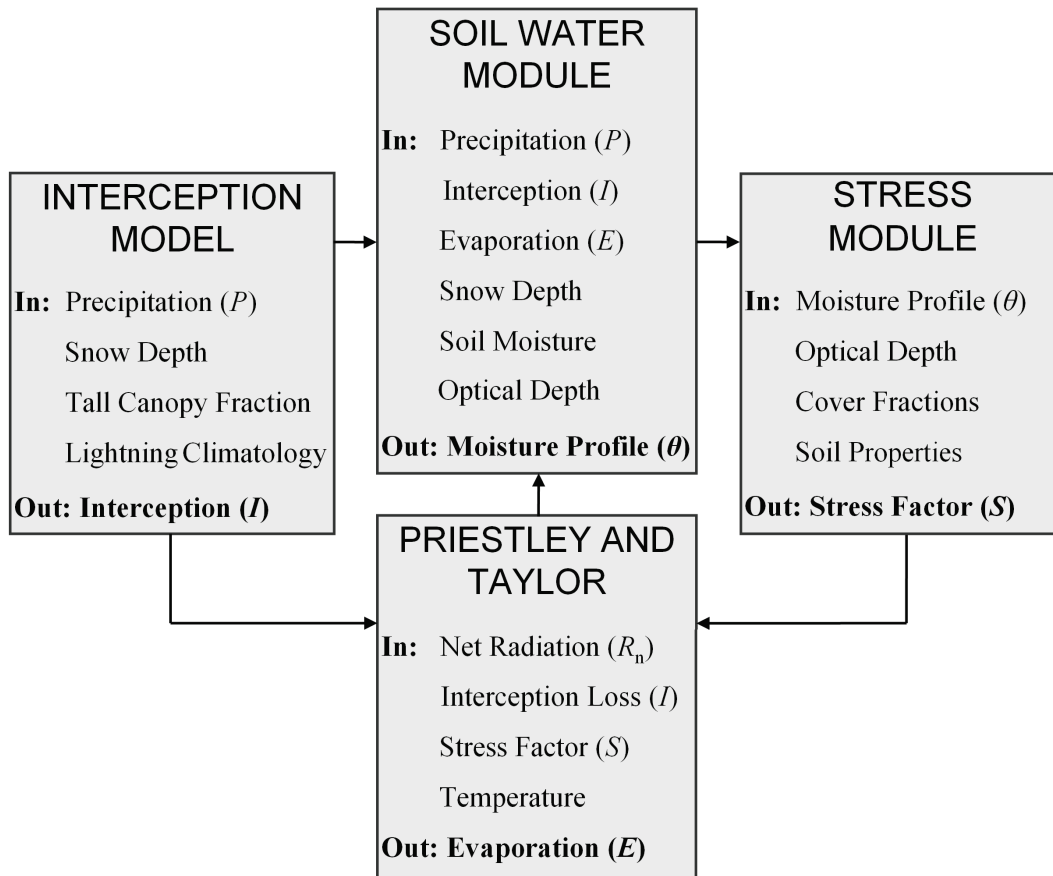Full Screen / Esc

Printer-friendly Version

Interactive Discussion

Table 2. Total precipitation (P), evaporation (E) and water available for runoff ($P-E$) divided by continents for the period 2003–2007. The contribution of rainfall interception loss (I) to E is also presented.

Continent	P	E			$P-E$			I		
	mm	mm	10^3 km^3	%P	mm	10^3 km^3	%P	mm	10^3 km^3	%P
Africa	930	547	16.2	59	383	11.4	41	38	1.1	4
Antarctica	199	21	0.3	11	177	2.5	89	0	0.0	0
Asia	638	382	16.5	60	256	11.1	40	35	1.5	5
Europe	592	344	3.3	58	247	2.3	42	39	0.4	7
N. America	639	405	9.3	63	234	5.4	37	35	0.8	5
Oceania	794	523	4.6	66	272	2.4	34	50	0.4	6
S. America	1706	964	17.0	57	742	13.0	43	144	2.5	8
Total	788	458	67.2	58	329	48.1	42	47	6.8	6

Table 3. Total precipitation (P), evaporation (E), water available for runoff ($P-E$) and rainfall interception loss (I) per biome type for 2003–2007.

Biome	P	E			$P-E$			I		
	mm	mm	$10^3\,\mathrm{km}^3$	%P	mm	$10^3\,\mathrm{km}^3$	%P	mm	$10^3\,\mathrm{km}^3$	%P
Tropical forest	2248	1182	19.7	53	1066	17.6	47	232	3.9	10
Temperate forest	668	495	4.5	74	174	1.6	26	84	0.8	13
Boreal forest	596	346	2.7	58	250	2.0	42	49	0.4	8
Shrubland	494	310	8.1	63	184	4.8	37	7	0.2	1
Savanna	1336	807	14.6	60	529	9.6	40	49	0.9	4
Grassland	677	460	4.2	68	217	2.0	32	14	0.1	2
Cropland	844	535	10.6	63	308	6.1	37	29	0.6	3
Permanent snow	226	27	0.4	12	199	3.3	88	0	0.0	0
Desert	162	110	2.5	68	52	1.2	32	0	0.0	0
TOTAL	788	458	67.2	58	329	48.1	42	47	6.8	6

INTERCEPTION MODEL

In: Precipitation (P)

    Snow Depth

    Tall Canopy Fraction

    Lightning Climatology

Out: Interception (I)

SOIL WATER MODULE

In: Precipitation (P)

    Interception (I)

    Evaporation (E)

    Snow Depth

    Soil Moisture

    Optical Depth

Out: Moisture Profile (θ)

STRESS MODULE

In: Moisture Profile (θ)

    Optical Depth

    Cover Fractions

    Soil Properties

Out: Stress Factor (S)

PRIESTLEY AND TAYLOR

In: Net Radiation (R_n)

    Interception Loss (I)

    Stress Factor (S)

    Temperature

Out: Evaporation (E)

Fig. 1. Schematic overview of GLEAM (adapted from Miralles et al., 2010b).
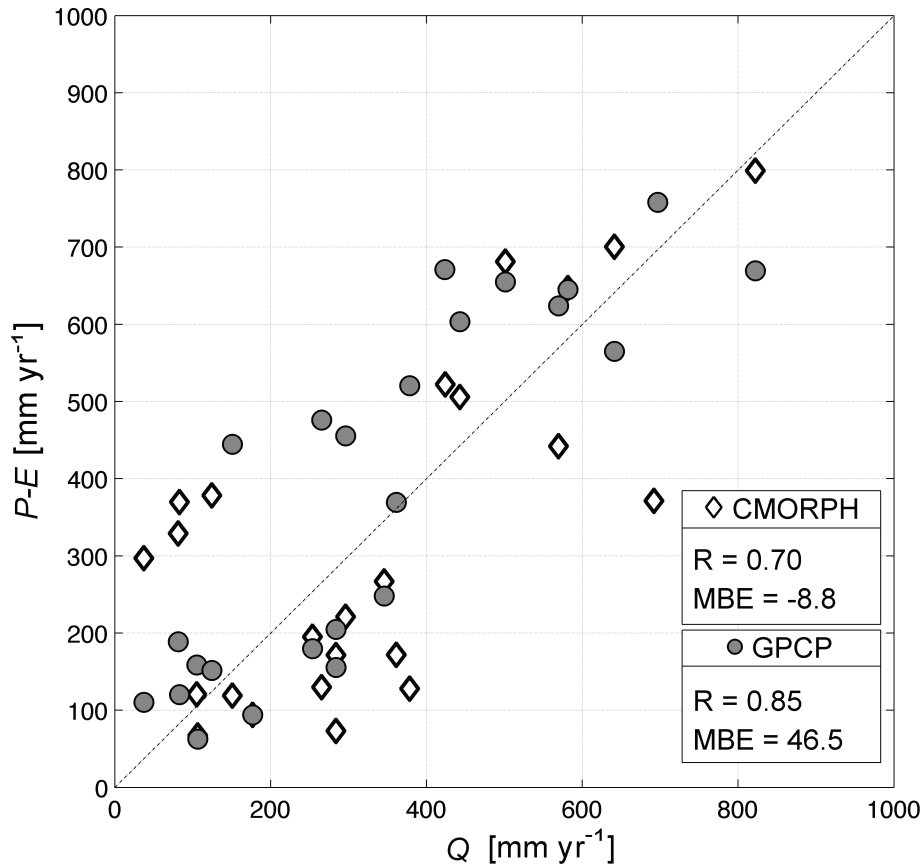
Fig. 2. GLEAM estimates of $P-E$ are compared to the runoff (Q) from 24 different catchments for the period 2003–2006. Correlation coefficients (R) and mean bias errors (MBE) are listed for both the validation exercise using GPCP and the one using CMORPH (gap-filled with GPCP as explained in Sect. 3).

Title Page

Abstract | Introduction

Conclusions | References

Tables | Figures

◄◄ | ►►

◄ | ►

Back | Close

Full Screen / Esc

Printer-friendly Version

Interactive Discussion
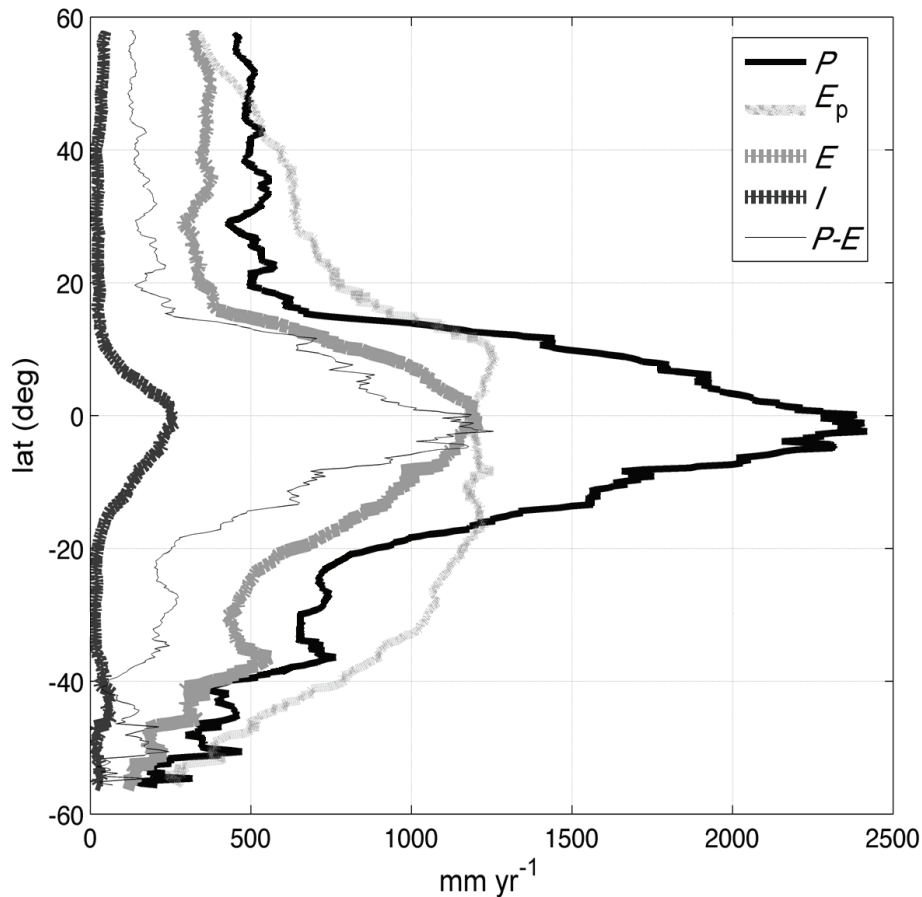
Fig. 3. Magnitude of the different hydrological fluxes as average along the latitudinal bands (modified from Fisher et al., 2008). The results correspond to the application of GLEAM for the period 2003–2007. E_p refers to potential evaporation.
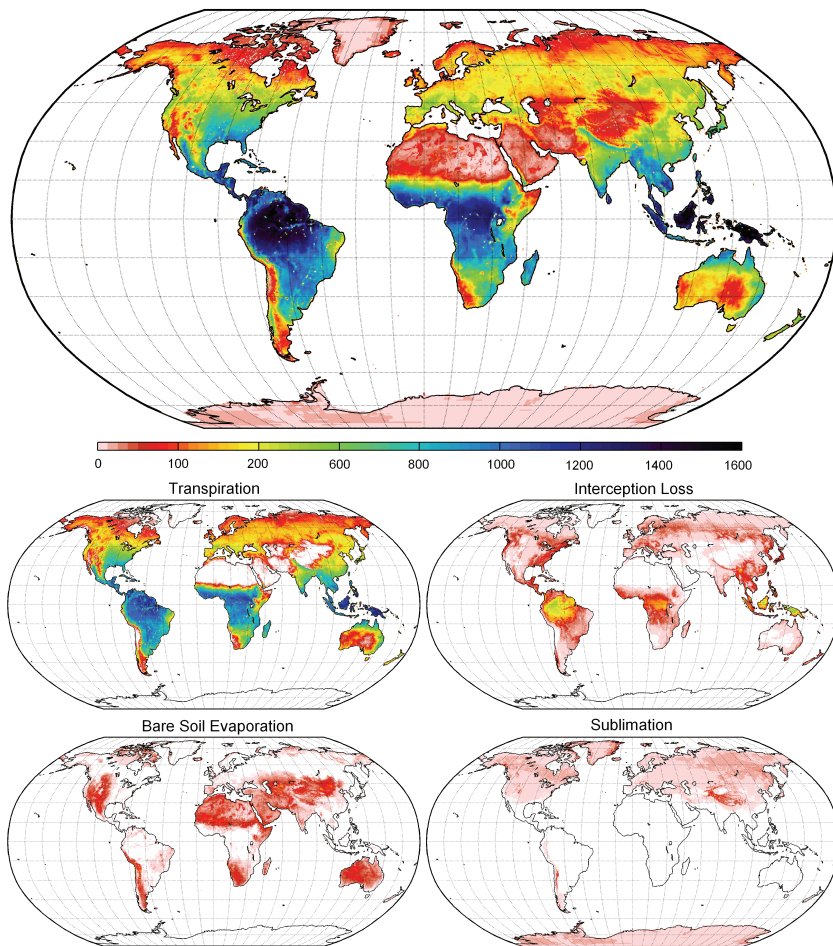
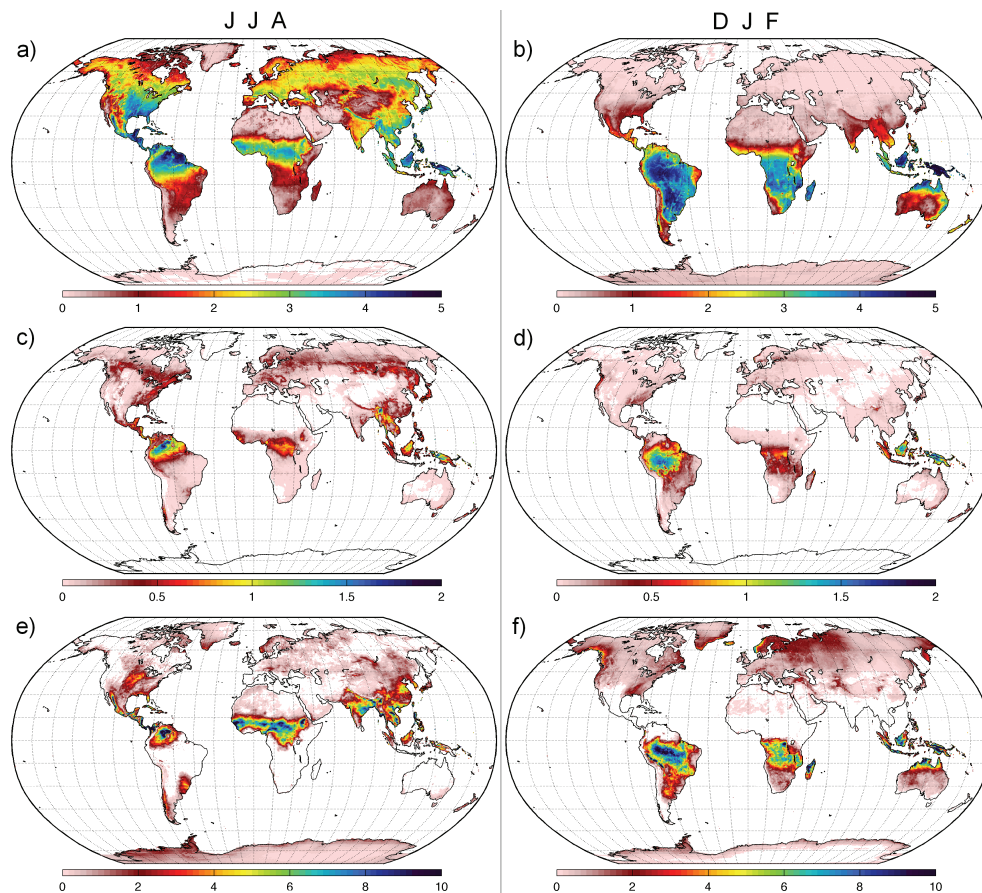**Fig. 4.** Decomposition of 2003–2007 average annual evaporation (mm) into its different contributing fluxes.

Fig. 5. Average fluxes for the period 2003–2007 in mm day^{-1} separately presented for JJA (left panel) and DJF (right panel): **(a)** and **(b)** show the distribution of E, **(c)** and **(d)** represent I, and **(e)** and **(f)** present the estimated distribution of $P-E$.
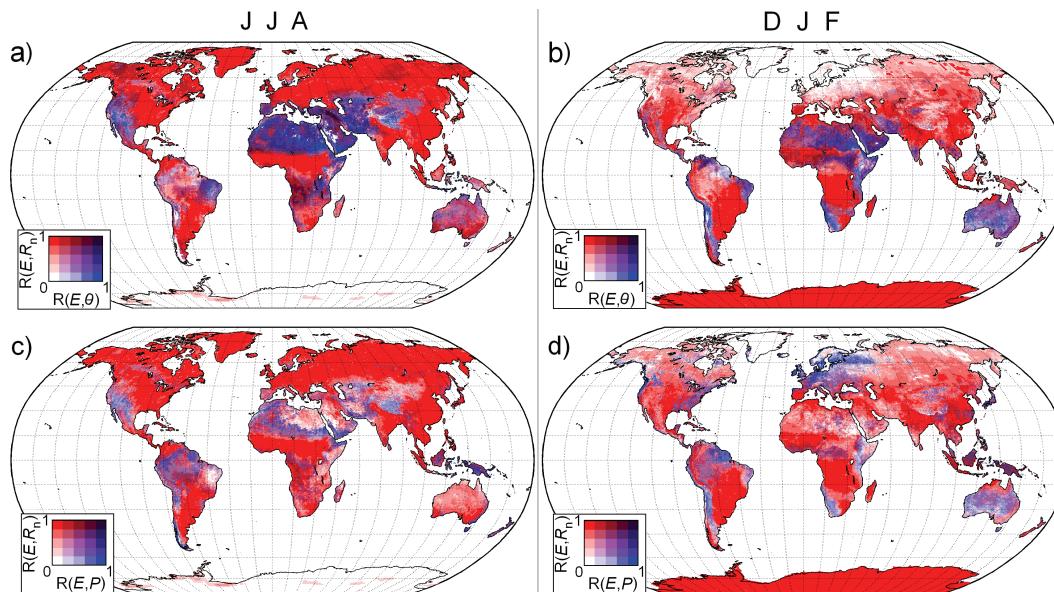
Fig. 6. The upper panel shows the estimated correlation (R) of daily time series of E with R_n and θ for JJA Fig. 5a and DJF Fig. 5b. The bottom figures show the correlation of daily E with R_n and P during JJA Fig. 5c and DJF Fig. 5e. All the results correspond to the period 2003–2007.